Supplemental Material for

Enhancing high harmonic generation in GaAs by elliptically polarized light excitation

Fumiya Sekiguchi[1], Minoru Sakamoto[1], Kotaro Nakagawa[1], Hirokazu Tahara[1,2], Shunsuke. A. Sato[3,4], Hideki Hirori[1], and Yoshihiko Kanemitsu[1]

[1]*Institute for Chemical Research, Kyoto University, Uji, Kyoto 611-0011, Japan*
[2]*The Hakubi Center for Advanced Research, Kyoto University, Kyoto 606-8501, Japan*
[3]*Center for Computational Sciences, University of Tsukuba, Tsukuba 305-8577, Japan*
[4]*Max Planck Institute for the Structure and Dynamics of Matter, Luruper Chaussee 149, 22761 Hamburg, Germany*

S1. Methods

The high harmonics (HHs) were measured in the reflection geometry. A schematic image of the experimental setup is shown in Fig. S1. The sample was undoped bulk GaAs with a (100) crystal surface. Mid-infrared (MIR) pulses with an energy of 0.37-eV (3.4 μm in wavelength) and pulse duration of ~ 70 fs were used for the excitation. The MIR pulses were generated by an optical parametric amplifier with a Ti:Sapphire regenerative amplifier (center wavelength: 800 nm, pulse energy: 2 mJ, duration: 35 fs, repetition rate: 5 kHz) as the pump source. The excitation pulses irradiated the sample almost normally, at about 5º angle of incidence. The pulses were focused onto the sample surface; the spot size was ~100 μm in diameter. The intensity of the excitation pulses was controlled by a pair of wire-grid (WG) polarizers, with another WG polarizer placed after the WG pair to ensure the linear polarization of the transmitted pulses. Note that the E_{exc}-field strengths described in this paper are the values inside the GaAs crystal. The polarization state of the excitation pulses was controlled by rotating a quarter-wave plate (QWP). The relation between the QWP angle and the excitation polarization, i.e., ε_{exc} and major-axis direction, was carefully measured. The angle θ between the major-axis direction of E_{exc} and the [100] crystal axis was controlled by rotating the GaAs crystal. While measuring the ε_{exc} dependence, θ was actively controlled so that it stayed constant. The polarization state of the HHs was measured by rotating the wire grid polarizer before the detection by the spectrometer and CCD. The difference of detection efficiency between the vertically- and horizontally-polarized HHs were taken into account.

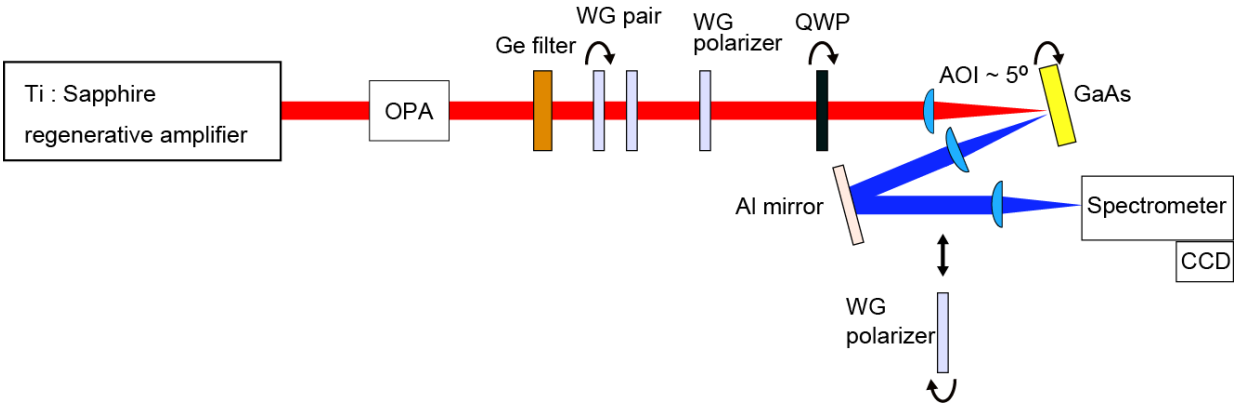

FIG. S1. Schematic experimental setup. OPA: optical parametric amplifier. WG: wire grid polarizer. QWP: quarter-wave plate. AOI: angle of incidence. CCD: charge coupled device.

S2. ε_{exc} dependence of HHG at $\theta = 0^{o}$, i.e., when the major axis of the excitation polarization is along the [100] direction

At strong E_{exc} fields around 7-8 MV/cm, the most efficient HHG by linear E_{exc} occurs at $\theta = 22.5^{o}$, as shown in Fig. 3 in the main text. On the other hand, at lower E_{exc} fields around 4-5 MV/cm, the most efficient HHG by linear E_{exc} occurs at $\theta = 0^{o}$. As a supplement to the data at $\theta = 22.5^{o}$ shown in Fig. 2 in the main text, we show here the ε_{exc} dependence of HHG at $\theta = 0^{o}$, where the major axis of the E_{exc} polarization is along the [100] direction.

As shown in Figs. S2(a) and S2(b), at a weak E_{exc} of 4.8 MV/cm, the elliptical E_{exc} yields smaller HH intensities compared with the linear E_{exc}. On the other hand, at a strong E_{exc} of 8.1 MV/cm, while the elliptical E_{exc} yields smaller intensities for the 5th, 7th and 13th HHs, it yields larger intensities for the 9th and 11th HH. More detailed ε_{exc} dependences are shown in Figs. S2(c) and S2(d). Fig. S2(c) shows the ε_{exc} dependence of the 11th HH at different E_{exc}-field strengths. As the E_{exc}-field strength increases, the magnitude of the elliptical enhancement becomes larger until it takes a maximum at 7.6 MV/cm. However, applying a further stronger E_{exc} field of 8.5 MV/cm leads to suppression of the elliptical enhancement. Figure S2(d) shows the ε_{exc} dependence of the 7th, 9th and 11th HH at an E_{exc} field of 7.4 MV/cm. A clear HH-order dependence can be identified in Fig. S2(d). These behaviors are the same as those observed at $\theta = 22.5^{o}$ in the main text.

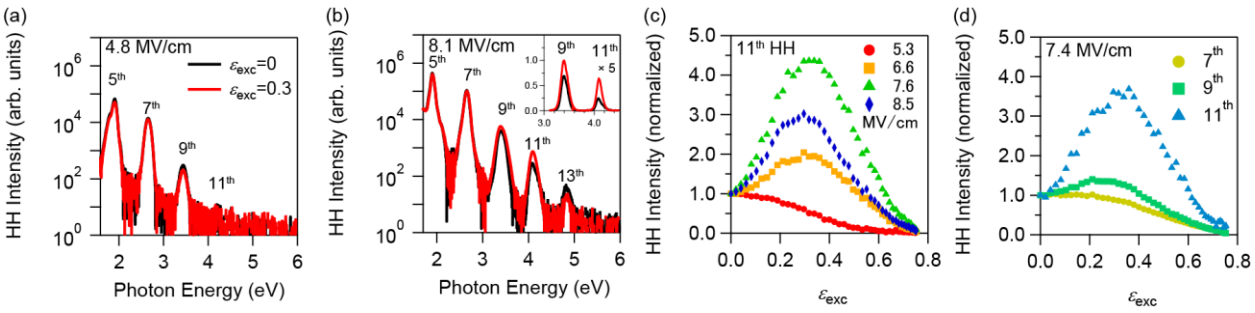

FIG. S2. (a,b) HH spectra generated by linear (ε_{exc} = 0) and elliptical (ε_{exc} = 0.3) excitations at E_{exc}-field strengths of (a) 4.8 MV/cm and (b) 8.1 MV/cm. (c) ε_{exc} dependence of the 11th HH yield, normalized by the value at ε_{exc} = 0 for different E_{exc}-field strengths. (d) ε_{exc} dependence of the 7th, 9th and 11th HH yield at E_{exc} = 7.4 MV/cm normalized by the value at ε_{exc} = 0.

S3. ε_{exc} dependence of HH yields for different θ

The emergence of the elliptical enhancement is accompanied by nonlinear optical activity, as shown in Fig. 3 in the main text. For another view of the nonlinear optical activity, we show the ε_{exc} dependence of the 9th- and 11th-HH intensities at E_{exc} = 8.0 MV/cm, measured at different θ, in Fig. S3. When the major axis of E_{exc} is oriented to a high-symmetry crystal direction, i.e., θ = 0º and 45º, the ε_{exc} dependence forms a symmetric curve for positive and negative helicities. On the other hand, when the major axis of E_{exc} is not along these high-symmetric crystal orientations, i.e., θ is somewhere between 0º and 45º, the ε_{exc} dependence becomes asymmetric with a pronounced enhancement at one side of helicity. This is a clear evidence of nonlinear elliptical dichroism, and it provides a complementary view to that of Fig. 3 in the main text.

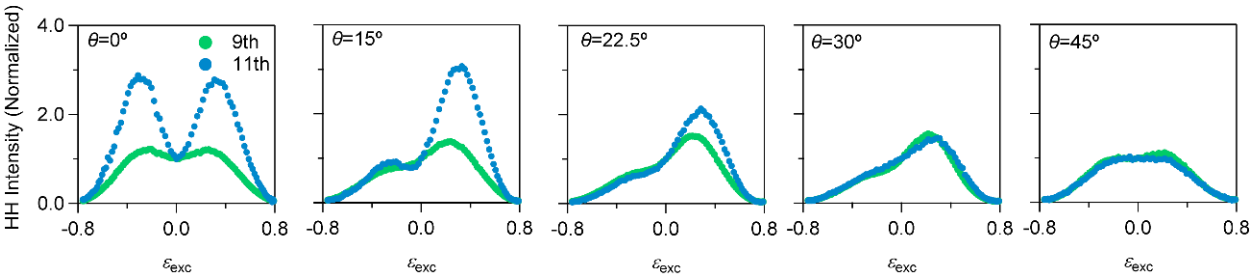

FIG. S3. ε_{exc} dependence of the 9th and 11th HH yield at E_{exc} = 8.0 MV/cm, at θ of 0º, 15º, 22.5º, 30º and 45º.

S4. Magnitude of elliptical enhancement for different θ

A quantity called the "enhancement ratio" is used to describe the magnitude of the elliptical enhancement: it is the ratio between the maximum HH intensity reached in the ε_{exc} dependence and the HH intensity at $\varepsilon_{exc} = 0$. In other words, the enhancement ratio corresponds to the maximum value of the ε_{exc} dependence curves, such as in Figs. 2(c) and 2(d) and in Fig. S3. A complete dataset of this enhancement ratio for 5th-13th HHs, measured at $\theta = 0^{\circ}$ and 22.5°, is shown in Fig. S4.

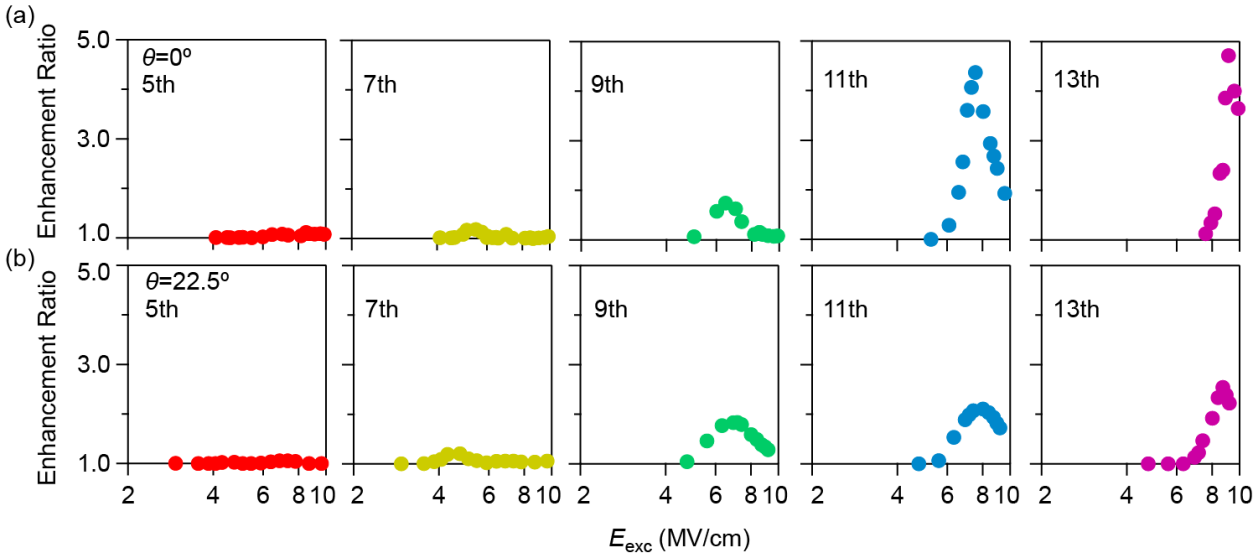

FIG. S4. E_{exc}-field-strength dependence of the enhancement ratio measured at (a) $\theta = 0^{\circ}$ and (b) $\theta = 22.5^{\circ}$.

S5. Microscopic electron dynamics simulation

Here, we briefly describe the numerical methods to describe the light-induced electron dynamics in GaAs for the analysis of HHG. The details of the methods are described in elsewhere [1,2]. To describe the light-induced electron dynamics under a homogeneous vector potential $\boldsymbol{A}(t)$, we employ the following quantum master equation for the one-body density matrix $\rho_{\boldsymbol{k}}(t)$ at each Bloch wavevector, $\boldsymbol{k}$,

$$\frac{d}{dt}\rho_{\boldsymbol{k}}(t) = \frac{\left[H_{\boldsymbol{k}+e\boldsymbol{A}(t)/\hbar}, \rho_{\boldsymbol{k}}(t)\right]}{i\hbar} + \widehat{D}[\rho_{\boldsymbol{k}}(t)], \qquad (S1)$$

where $H_{\boldsymbol{k}}(t)$ is the one-body Hamiltonian with the wavevector shift with the acceleration theorem: $k \to k + e\boldsymbol{A}(t)/\hbar$. To describe the electronic structure of GaAs, we employ the *sp*3*d*5*s** tight-binding model parameterized by the ab-initio simulations [3]. In the tight-binding model, each Ga and As atom consists of 10 atomic orbitals (one *s*-orbital + three *p*-orbitals + five *d*-orbitals + one *s**-orbital, where *s** is an additional *s*-orbital for the improved electronic structure description [4,5]), the GaAs primitive cell therefore consists of 20 atomic orbitals. The resulting electronic structure is described by four spin-degenerate valence bands and 16 spin-degenerate conduction bands. In Eq. $(S1)$, $\widehat{D}[\rho_{\boldsymbol{k}}(t)]$ denotes the relaxation operator. In this work, we employ the relaxation time approximation for the relaxation operator. For practical calculations, we employ the following form for the relaxation operator:

$$\widehat{D}[\rho_{\boldsymbol{k}}(t)] = -\sum_{b} \frac{\rho_{bb,\boldsymbol{k}}(t) - f_b^{ref}}{T_1} \left|u_{b\boldsymbol{k}}^H(t)\right\rangle\left\langle u_{b\boldsymbol{k}}^H(t)\right| - \sum_{b\neq b'} \frac{\rho_{bb',\boldsymbol{k}}(t)}{T_2} \left|u_{b\boldsymbol{k}}^H(t)\right\rangle\left\langle u_{b'\boldsymbol{k}}^H(t)\right|, \qquad (S2)$$

where b is the band index, and $\left|u_{b\boldsymbol{k}}^H(t)\right\rangle$ is an instantaneous eigenstate of the Hamiltonian, $H_{\boldsymbol{k}+e\boldsymbol{A}(t)/\hbar}$, as $H_{\boldsymbol{k}+e\boldsymbol{A}(t)/\hbar}\left|u_{b\boldsymbol{k}}^H(t)\right\rangle = \epsilon_{b\boldsymbol{k}}^H(t)\left|u_{b\boldsymbol{k}}^H(t)\right\rangle$. The matrix elements, $\rho_{bb',\boldsymbol{k}}(t)$, is defined as $\rho_{bb',\boldsymbol{k}}(t) = \left\langle u_{b\boldsymbol{k}}^H(t)\middle|\rho_{\boldsymbol{k}}(t)\middle|u_{b'\boldsymbol{k}}^H(t)\right\rangle$. Here, f_b^{ref} is a reference occupation factor, and it is one for the valence bands ($b = v$), and zero for the conduction bands ($b = c$). The first term of the relaxation operator in Eq. $(S2)$ describes the longitudinal relaxation, and the corresponding decay constant is given by T_1. The second term describes the transverse relaxation, or namely the decoherence, and its decay time is given by T_2. In this work, we set T_1 to 3 ps, and T_2 to 20 fs.

By employing the time-dependent density matrix $\rho_{\boldsymbol{k}}(t)$, one can evaluate the electric current with the following expression

$$\boldsymbol{J}(t) = -\frac{e}{m_e\hbar(2\pi)^3}\int_{BZ} d\boldsymbol{k}\,\mathrm{Tr}\left[\frac{\partial H_{\boldsymbol{k}+e\boldsymbol{A}(t)/\hbar}}{\partial \boldsymbol{k}}\rho_{\boldsymbol{k}}(t)\right]. \qquad (S3)$$

Furthermore, by applying the Fourier transform to the induced current, $\boldsymbol{J}(t)$, one can evaluate the yield of the emitted harmonics as

$$I_{HHG}(\omega) = \omega^2\left|\int_{-\infty}^{\infty} dt\,\boldsymbol{J}(t)\,e^{i\omega t}\right|^2. \qquad (S4)$$

For practical simulations in this work, we employ the following form for the vector potential

$$\boldsymbol{A}(t) = -\frac{E_0}{\omega_0}\frac{1}{\sqrt{1+\epsilon_{ext}^2}}\boldsymbol{e}_p \sin(\omega_0 t)\cos^4\left[\frac{\pi}{T_0}t\right] - \frac{E_0}{\omega_0}\frac{\epsilon_{ext}}{\sqrt{1+\epsilon_{ext}^2}}\bar{\boldsymbol{e}}_p \cos(\omega_0 t)\cos^4\left[\frac{\pi}{T_0}t\right] \quad (S5)$$

in the domain $-T_0/2 < t < T_0/2$, and zero outside this domain. Here, E_0 is the peak electric field strength, ω_0 is the mean frequency, and T_0 is the full duration of the pulse. In this work, we set E_0 to 8 MV/cm, ω_0 to 0.365 eV/$\hbar$, and T_0 to 200 fs. Note that the full duration of 200 fs corresponds to 52 fs as the full-width-of-half-maximum of the laser intensity, which is consistent with the experimental pulse width of 70 fs. The polarization vector $\boldsymbol{e}_p$ is set to the direction of θ= 22.5°, while $\bar{\boldsymbol{e}}_p$ is set to the direction of θ= 112.5°. Hence, the parameter ϵ_{ext} corresponds to the ellipticity of the light.

To investigate the HHG from GaAs, we compute the electron dynamics under the vector potential given in Eq. ($S5$) by solving the quantum master equation, Eq. ($S1$), and evaluate the induced current with Eq. ($S3$), resulting in the emitted harmonic intensity via Eq. ($S4$). Furthermore, we evaluate each harmonic intensity by integrating $I_{HHG}(\omega)$ within the finite photon energy range as

$$I_{HHG}^{n} = \int_{\omega_0\left(n-\frac{1}{2}\right)}^{\omega_0\left(n+\frac{1}{2}\right)} d\omega\, I_{HHG}(\omega). \quad (S6)$$

Figure 8 in the main text shows the 9th order harmonic intensity as a function of the ellipticity, ϵ_{ext}.

Having described the numerical methods to analyze HHG from GaAs, we further introduce the band-freezing analysis method in order to elucidate contributions to HHG from each band. For this purpose, we first discuss the approximated propagator for Eq. ($S1$). To propagate the density matrix, $\rho_{\boldsymbol{k}}(t)$, from t to $t+\Delta t$, we take the following three steps:

(*First step*)
In the first step of the propagation, we approximately evaluate the contribution from the relaxation operator for the propagation from t to $t+\Delta t/2$. The resulting density matrix is given by

$$\tilde{\rho}_{\boldsymbol{k}}(t) = \sum_{jk} \left|u_{j\boldsymbol{k}}^{H}(t)\right\rangle \tilde{\rho}_{jk,\boldsymbol{k}}(t) \left\langle u_{k\boldsymbol{k}}(t)\right|. \quad (S7)$$

Here, the matrix elements, $\tilde{\rho}_{jk,\boldsymbol{k}}$, in the instantaneous eigenbasis expression are given by

$$\tilde{\rho}_{jk,\boldsymbol{k}}(t) = \begin{cases} f_j + \left(\rho_{jk,\boldsymbol{k}}(t) - f_j\right)e^{-\Delta t/2T_1} & \text{for } j = k \\ \rho_{jk,\boldsymbol{k}}(t)e^{-\Delta t/2T_2} & \text{otherwise.} \end{cases}$$

(*Second step*)
In the second step, the relaxation free propagation from t to $t+\Delta t$ is approximately evaluated as

$$\tilde{\rho}_{\boldsymbol{k}}(t+\Delta t) = e^{-\frac{i\Delta t}{2\hbar}H_{\boldsymbol{k}+e\boldsymbol{A}(t+\Delta t)}} e^{-\frac{i\Delta t}{2\hbar}H_{\boldsymbol{k}+e\boldsymbol{A}(t)}} \tilde{\rho}_{\boldsymbol{k}}(t) e^{+\frac{i\Delta t}{2\hbar}H_{\boldsymbol{k}+e\boldsymbol{A}(t)}} e^{+\frac{i\Delta t}{2\hbar}H_{\boldsymbol{k}+e\boldsymbol{A}(t+\Delta t)}}$$

$$= \sum_{jklm} \left|u_{l\boldsymbol{k}}^{H}(t)\right\rangle\left\langle u_{m\boldsymbol{k}}^{H}(t)\right| U_{lj,\boldsymbol{k}}(t)\, \tilde{\rho}_{jk,\boldsymbol{k}}(t) U_{mk,\boldsymbol{k}}^{*}(t), \qquad (S8)$$

where the matrix elements, $U_{lj,\boldsymbol{k}}(t)$, are defined as

$$U_{lj,\boldsymbol{k}}(t) = \left\langle u_{l\boldsymbol{k}}^{H}(t+\Delta t)\middle| u_{j\boldsymbol{k}}^{H}(t)\right\rangle e^{-\frac{i}{2}\left(\epsilon_{l\boldsymbol{k}}^{H}(t+\Delta t)+\epsilon_{j\boldsymbol{k}}^{H}(t)\right)}. \qquad (S9)$$

Here, the matrix elements, $U_{lj,\boldsymbol{k}}(t)$, describes the nonadiabatic coupling between different bands. Therefore, one can artificially truncate the interband transitions by the corresponding matrix elements to zero, omitting the nonadiabatic coupling. We will use this degree of freedom for the frozen-band analysis.

(*Third step*)
In the third step, the residual relaxation contribution is evaluated for the propagation from $t + \Delta/2$ to $t + \Delta t$. The resulting density matrix is given by

$$\rho_{\boldsymbol{k}}(t+\Delta t) = \sum_{jk} \left|u_{j\boldsymbol{k}}^{H}(t+\Delta t)\right\rangle \rho_{jk,\boldsymbol{k}}(t+\Delta t) \left\langle u_{k\boldsymbol{k}}(t+\Delta t)\right|. \qquad (S7)$$

Here, the matrix elements, $\rho_{jk,\boldsymbol{k}}(t+\Delta t)$, in the instantaneous eigenbasis expression are given by

$$\rho_{jk,\boldsymbol{k}}(t+\Delta t) = \begin{cases} f_j + \left(\tilde{\rho}_{jk,\boldsymbol{k}}(t+\Delta t) - f_j\right) e^{-\Delta t/2T_1} & \text{for } j = k \\ \tilde{\rho}_{jk,\boldsymbol{k}}(t+\Delta t) e^{-\Delta t/2T_2} & \text{otherwise.} \end{cases}$$

By employing the above three steps, the density matrix, $\rho_{\boldsymbol{k}}(t)$, can be approximately propagated from t to $t + \Delta t$. Note that, this approximated propagation becomes exact in the small time step limit; $\Delta t \to 0$.

Among various approximated propagators, the above choice is suitable for analyzing the contribution to HHG from each band because dynamics of certain bands can be frozen by omitting the off-diagonal elements of $U_{lj,\boldsymbol{k}}(t)$ and terminating the interband transitions. For example, by omitting all the off-diagonal elements of $U_{lj,\boldsymbol{k}}(t)$, all the interband transitions are removed from the calculations. Similarly, by omitting all the off-diagonal elements except those among the top valence and bottom conduction bands, one can omit the contributions from all the bands except the top valence and bottom conduction bands. Figure 8 in the main text shows the 9th order harmonic intensity by including only a part of the bands in the simulation.

References

[1] S. A. Sato, J. W. McIver, M. Nuske, P. Tang, G. Jotzu, B. Schulte, H. Hübener, U. De Giovannini, L. Mathey, M. A. Sentef, A. Cavalleri, and A. Rubio, Microscopic theory for the light-induced anomalous Hall effect in graphene. *Phys. Rev. B* **99**, 214302 (2019).

[2] Wenwen Mao, Angel Rubio, and Shunsuke A. Sato, Terahertz-induced high-order harmonic generation and nonlinear charge transport in graphene. *Phys. Rev. B* **106**, 024313 (2022).

[3] Y. Tan, M. Povolotskyi, T. Kubis, Y. He, Z. Jiang, G. Klimeck, T. B. Boykin, Empirical tight binding parameters for GaAs and MgO with explicit basis through DFT mapping. *J. Comput. Electron*. **12**, 56 (2013).

[4] P. Vogl, Harold P. Hjalmarson, John D. Dow, A Semi-empirical tight-binding theory of the electronic structure of semiconductors. *J. Phys. Chem.* **44**, 365 (1983).

[5] J.-M. Jancu, R. Scholz, F. Beltram, F. Bassani, Empirical spds* tight-binding calculation for cubic semiconductors: General method and material parameters. *Phys. Rev. B* **57**, 6493 (1998).